


Exploring dark matter-gauge boson effective interactions at current and future colliders*

Yu Zhang (张宇)^{1,2} Yi-Wei Huang (黄祎伟)¹ Wei-Tao Zhang (张伟涛)³ Mao Song (宋昂)³ Ran Ding (丁然)^{3†} 

¹Institutes of Physical Science and Information Technology, Anhui University, Hefei 230601, China

²School of Physics, Hefei University of Technology, Hefei 230601, China

³School of Physics and Optoelectronics Engineering, Anhui University, Hefei 230601, China

Abstract: In this study, we systematically investigate collider constraints on effective interactions between Dark Matter (DM) particles and electroweak gauge bosons. We consider the simplified models in which scalar or Dirac fermion DM candidates couple only to electroweak gauge bosons through high dimensional effective operators. Considering the induced DM-quarks and DM-gluons operators from the Renormalization Group Evolution (RGE) running effect, we present comprehensive constraints on the effective energy scale Λ and Wilson coefficients $C_B(\Lambda)$, $C_W(\Lambda)$ from direct detection, indirect detection, and collider searches. In particular, we present the corresponding sensitivity from the Large Hadron Electron Collider (LHeC) and Future Circular Collider in the electron-proton mode (FCC-ep) for the first time, update the mono- j and mono- γ search limits at the Large Hadron Collider (LHC), and derive the new limits at the Circular Electron Positron Collider (CEPC).

Keywords: dark matter, effective field theory, LHC, CEPC, LHeC, FCC-ep

DOI: 10.1088/1674-1137/ad2362

I. INTRODUCTION

Observations from astrophysics and cosmology have provided overwhelming evidence for the existence of DM [1]. However, the microscopic properties of DM are still poorly known as all of such observations are based on its gravitational effects. Weakly Interacting Massive Particles (WIMPs) are canonical DM candidates. Such a scenario can easily fulfill the relic abundance through the thermal freeze-out mechanism (the “WIMP miracle”) [2] and can be naturally embedded in many popular theoretical frameworks [3, 4]. Moreover, owing to their weak interaction with SM particles, WIMPs can be probed through three experimental prongs, i.e., collider, direct, and indirect detections.

Typically, the interactions between DM and SM particles are model-dependent, and exploring the complete model landscape is significantly challenging. Instead of exhausting all possible theoretical model parameter spaces, the Effective Field Theory (EFT) framework is extensively used, which enables us to capture some key features of the high-scale physics effects on the electroweak scale while significantly simplifying the ana-

lysis procedures. For EFT collider searches, various signal channels based on different SM portal effective operators have been extensively studied at the hadron and electron colliders [5–34].

Among them, the parameter space of DM-quark interaction that fulfills the correct relic density has a conflict with the exclusion limits from direct detection, indirect detection, and collider searches. In this work, we consider dimension-6 (7) DM-diboson effective operators for scalar (Dirac fermion) DM and examine their sensitivity at the current LHC and future electron and electron-proton colliders. The current limits of DM-diboson operators at the LHC are primarily constrained by mono- j and mono- γ signal channels, and the mono- γ signature is a sensitive channel at the CEPC. The two most currently promising proposals for electron-proton colliders are the LHeC and FCC-ep. The LHeC is based on an economic LHC upgrade, and a 60–140 GeV electron beam is planned for collision with a 7 TeV proton beam in the LHC ring during the High Luminosity LHC (HL-LHC) run. The FCC-ep is designed to collide a 60 GeV electron with the 50 TeV proton beam. DM pairs can be pro-

Received 7 September 2023; Accepted 29 January 2024; Published online 30 January 2024

* RD is Supported in part by the National Key R&D Programme of China (2021YFC2203100). YZ is Supported in part by the National Natural Science Foundation of China (11805001) and the Fundamental Research Funds for the Central Universities (JZ2023HGTB0222)

† E-mail: dingran@mail.nankai.edu.cn



Content from this work may be used under the terms of the Creative Commons Attribution 3.0 licence. Any further distribution of this work must maintain attribution to the author(s) and the title of the work, journal citation and DOI. Article funded by SCOAP³ and published under licence by Chinese Physical Society and the Institute of High Energy Physics of the Chinese Academy of Sciences and the Institute of Modern Physics of the Chinese Academy of Sciences and IOP Publishing Ltd

duced through the VBF process with a cleaner background, which corresponds to a $\cancel{E}_T + e^- j$ signal.

The remainder of this paper is organized as follows. In Sec. II, we briefly describe the DM-diboson effective operators. Subsequently, the relevant collider phenomenology of the $\cancel{E}_T + e^- j$ signal channel at the LHeC and FCC-ep is discussed in Sec. III, including event simulations, kinematical distributions of final states, and cut selections related to signals and backgrounds. In Sec. IV, we present the sensitivity at the CEPC with a mono- γ signature. The limits from the LHC with current mono- j and mono- γ searches are updated in Sec. V. The constraints from current direct and indirect DM search experiments are discussed in Sec. VI. The results are presented in Sec. VII. Finally, we provide a summary and conclusion in Sec. VIII.

II. FRAMEWORK OF DM-GAUGE BOSON EFFECTIVE INTERACTIONS

We consider the DM particle as a Dirac fermion (χ) or scalar (ϕ) that connects with a SM sector through high-dimensional DM-gauge boson effective operators. At the lowest order, such operators enable DM to couple with a single gauge boson, which induces electromagnetic dipole and anapole interactions [35, 36]. However, these interactions lead to monochromatic gamma-rays when the unsuppressed cross-section of DM annihilates into the $\gamma\gamma$ and γZ modes, which are severely constrained by current indirect detection experiments [37]. Thus, we start from DM-diboson operators:

$$\mathcal{O}_B^\phi = \phi^* \phi B^{\mu\nu} B_{\mu\nu}, \quad \mathcal{O}_W^\phi = \phi^* \phi W^{a,\mu\nu} W_{\mu\nu}^a, \quad (1)$$

$$\mathcal{O}_B^\chi = \bar{\chi} \chi B^{\mu\nu} B_{\mu\nu}, \quad \mathcal{O}_W^\chi = \bar{\chi} \chi W^{a,\mu\nu} W_{\mu\nu}^a. \quad (2)$$

These operators are assumed to be generated at the energy scale Λ , with other high energy resonances much heavier than Λ being all decoupled. Note that in this scenario, the coupling between DM and the SM quarks can also be induced through the RGE from the Λ scale down to the electroweak scale μ_{EW} . Consequently, two extra dimension-6 (7) operators

$$\mathcal{O}_y^\phi = y_q \phi^* \phi \bar{q} H q, \quad \mathcal{O}_H^\phi = \phi^* \phi (H^\dagger H)^2, \quad (3)$$

$$\mathcal{O}_y^\chi = y_q \bar{\chi} \chi \bar{q} H q, \quad \mathcal{O}_H^\chi = \bar{\chi} \chi (H^\dagger H)^2, \quad (4)$$

must be considered. In the above equations, $y_q = \sqrt{2} m_q / v$ denotes the Yukawa couplings of SM quarks, and v is the

vacuum expectation value (VEV) of the SM Higgs doublet H . Subsequently, the total effective Lagrangian at scale μ ($\mu_{EW} < \mu < \Lambda$) is given by

$$\mathcal{L}_{\text{eff}}^{\phi,\chi} = \sum_{k=B,W,Y,H} \frac{C_k^{\phi,\chi}(\mu)}{\Lambda^2} \mathcal{O}_k. \quad (5)$$

At the leading logarithmic (LL) order, the Wilson coefficients of the effective operators \mathcal{O}_y and \mathcal{O}_H at the scale μ_{EW} are [38]

$$C_y(\mu_{EW}) \simeq \frac{6Y_{qL}Y_{qR}\alpha_1}{\pi} \ln\left(\frac{\mu_{EW}}{\Lambda}\right), \quad (6)$$

$$C_H(\mu_{EW}) \simeq -9\alpha_2^2 \ln\left(\frac{\mu_{EW}}{\Lambda}\right) C_W(\Lambda), \quad (7)$$

where $Y_{qL}(Y_{qR})$ denotes the hypercharges of the left-handed (right-handed) quarks with $Y_{uL} = Y_{dL} = 1/6$, $Y_{uR} = 2/3$, and $Y_{dR} = 1/3$, and α_1 and α_2 are the gauge coupling constants of the $U(1)_Y$ and $SU(2)_Y$ gauge groups, respectively. In our calculation, we set $\mu_{EW} \equiv m_Z$ with $\alpha_1 \simeq 1/98$ and $\alpha_2 \simeq 1/29$. After electroweak symmetry breaking (EWSB), the gauge eigenstate fields B_μ and W_μ^3 mix into the physical massless photon field A_μ and massive gauge field Z_μ . Subsequently, the effective DM-diboson and DM-quark operators are recast as

$$\begin{aligned} \mathcal{O}_{FF}^\phi &= \phi^* \phi F^{\mu\nu} F_{\mu\nu}, & \mathcal{O}_{FF}^\chi &= \bar{\chi} \chi F^{\mu\nu} F_{\mu\nu}, \\ \mathcal{O}_q^\phi &= m_q \phi^* \phi \bar{q} q, & \mathcal{O}_q^\chi &= m_q \bar{\chi} \chi \bar{q} q, \end{aligned} \quad (8)$$

where $FF = AA, AZ, ZZ, WW$. The relevant matching conditions are

$$\begin{aligned} C_{AA}(\mu_{EW}) &= C_B(\mu_{EW}) \cos^2 \theta_W + C_W(\mu_{EW}) \sin^2 \theta_W, \\ C_{ZZ}(\mu_{EW}) &= C_W(\mu_{EW}) \cos^2 \theta_W + C_B(\mu_{EW}) \sin^2 \theta_W, \\ C_{AZ}(\mu_{EW}) &= (C_W(\mu_{EW}) - C_B(\mu_{EW})) \sin 2\theta_W, \\ C_{WW}(\mu_{EW}) &= C_W(\mu_{EW}), \\ C_q(\mu_{EW}) &= C_y(\mu_{EW}) - \frac{v^2}{m_h^2} C_H(\mu_{EW}), \end{aligned} \quad (9)$$

with θ_W is the Weinberg angle.

Integrating out the heavy top quarks, the effective DM-gluon operators

$$\mathcal{O}_q^\phi = \alpha_s \phi^* \phi G^{a,\mu\nu} G_{\mu\nu}^a, \quad \mathcal{O}_q^\chi = \alpha_s \bar{\chi} \chi G^{a,\mu\nu} G_{\mu\nu}^a \quad (10)$$

can be generated, where $G_{\mu\nu}^a$ denotes the gluon field strength. The matching condition at leading order is giv-

en by [39]

$$C_G(m_t) = -\frac{1}{12\pi} C_t(m_t). \quad (11)$$

When RGEs are evolved from the EW scale down to the hadronic scale $\mu_{\text{had}} \simeq 1$ GeV, O_{AA} will contribute to O_q through the exchanging of virtual photons. For scale μ with $m_q < \mu < \mu_{\text{EW}}$, we obtain [40]

$$C_q(\mu) \simeq C_q(\mu_{\text{EW}}) + \frac{6Q_q^2\alpha_{\text{em}}}{\pi} \ln\left(\frac{\mu}{\mu_{\text{EW}}}\right) C_{AA}(\mu_{\text{EW}}) \quad (12)$$

at the LL order, where Q_q is the electric charge of a quark, and the electromagnetic coupling constant $\alpha_{\text{em}} \simeq 1/137$.

At the m_b and m_c threshold, we must integrate out the corresponding heavy bottom and charm quarks by considering Eq. (11) again. At the scale $\mu_{\text{had}} \simeq 1$ GeV, we obtain

$$C_q(\mu_{\text{had}}) \simeq \left(\frac{6Y_{qL}Y_{qR}\alpha_1}{\pi} C_B(\Lambda) + 9\alpha_2^2 \frac{v^2}{m_h^2} C_W(\Lambda) \right) \ln\left(\frac{\mu_{\text{EW}}}{\Lambda}\right) + \frac{6Q_q^2\alpha_{\text{em}}}{\pi} C_{AA}(\mu_{\text{EW}}) \ln\left(\frac{\mu_{\text{had}}}{\mu_{\text{EW}}}\right), \quad (13)$$

$$C_G(\mu_{\text{had}}) \simeq -\frac{1}{12\pi} \left\{ \left(\frac{\alpha_1}{\pi} C_B(\Lambda) + 27\alpha_2^2 \frac{v^2}{m_h^2} C_W(\Lambda) \right) \ln\left(\frac{\mu_{\text{EW}}}{\Lambda}\right) + \frac{2\alpha_{\text{em}}}{3\pi} C_{AA}(\mu_{\text{EW}}) \left[\ln\left(\frac{m_b}{\mu_{\text{EW}}}\right) + 4\ln\left(\frac{m_c}{\mu_{\text{EW}}}\right) \right] \right\}, \quad (14)$$

where the Wilson coefficient $C_{AA}(\mu_{\text{EW}})$ is determined by the first matching condition in Eq. (9).

III. SENSITIVITIES AT THE LHEC AND FCC-EP

In this section, we investigate the sensitivity of the DM-gauge boson effective operators at future electron-proton colliders.

A. Signal channels and SM backgrounds

From the effective interactions in Eqs. (1) and (2), DM pairs can be produced at the electron-proton collider through both the Charged Current (CC) and Neutral Current (NC), which respectively correspond to the W boson and γ/Z modes of VBF processes. In CC production, DM can be generated through the process of $e^-p \rightarrow \nu_e j \chi \bar{\chi}(\phi\phi^*)$ via WW fusion, resulting in a mono-jet plus missing energy signature. Note that the mono-jet signature coincidentally aligns with the background of CC deeply inelastic scattering. Owing to the absence of kinematic handles in the final state, distinguishing this signal channel from its

primary background poses a significant challenge. Consequently, our study is primarily focused on NC production – specifically the process $e^-p \rightarrow e^- j \chi \bar{\chi}(\phi\phi^*)$, as depicted in Fig. 1. Thus, the corresponding signature is characterized as the $\cancel{E}_T + e^- j$ channel.

For SM background estimation, we consider both the reducible background (RB) and irreducible background (IB). The IB is primarily due to the processes $e^-p \rightarrow e^- j \nu_\ell \bar{\nu}_\ell$ ($\ell = e, \mu, \tau$). Among them, both W/Z -boson bremsstrahlung processes $e^-p \rightarrow e^- j Z/\nu_e j W^-$ ($Z \rightarrow \nu_e \bar{\nu}_e / W^- \rightarrow e^- \bar{\nu}_e$) contribute to ν_e final state, whereas for $\nu_{\mu,\tau}$, only the bremsstrahlung process $e^-p \rightarrow e^- j Z$ ($Z \rightarrow \nu_{\mu,\tau} \bar{\nu}_{\mu,\tau}$) is relevant. For the RB, a major contribution is from $e^-p \rightarrow e^- j W^\pm$ with a W leptonic decay $W^\pm \rightarrow \ell^\pm \nu_\ell$. Therefore, two possibilities must be considered. One is that electron and muon final states exceed the detector acceptance, and the τ final state mimics a hard jet in the detector. Another possibility is that the products of hadronic τ decays are too soft to be tagged [41, 42]. Consequently, the SM background can be summarized as follows:

- IB: $e^-p \rightarrow e^- j \nu_\ell \bar{\nu}_\ell$,
- RB: $e^-p \rightarrow e^- j \ell^\pm \nu_\ell(\bar{\nu}_\ell)$,

where $\ell = e, \mu, \tau$.

B. Event simulation and kinematical cuts

For an event simulation, we generate a Universal FeynRules Output (UFO) [43] model file using the FeynRules package [44], which is fed into MadGraph@NLO [45] to generate parton-level events. For both signal and backgrounds at the parton level, we apply the following *pre-selection cuts*:

$$p_T^{j,\ell} > 5 \text{ GeV}, \quad |\eta_{j,\ell}| < 5, \\ \Delta R_{j\ell} > 0.4, \quad \Delta R_{\ell\ell} > 0.4, \quad (15)$$

where p_T and η are the transverse momentum and pseudorapidity of the corresponding particles, respectively, and $\Delta R = \sqrt{\Delta\phi^2 + \Delta y^2}$ is the separation in the azimuthal angle-rapidity ($\phi-y$) plane. Note that all of the cuts in Eq. (15) are defined in the laboratory frame. We then use Pythia6.4 [46] to implement parton shower and hadroniz-

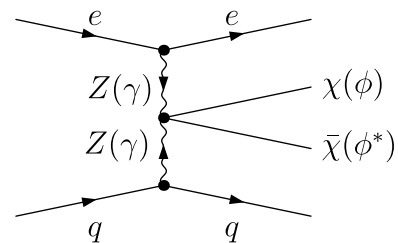


Fig. 1. Feynman diagram for the process $e^-p \rightarrow e^- j \chi \bar{\chi}(\phi\phi^*)$.

ation and Delphes3.4 [47] for rapid detector simulation according to the LHeC designed parameters [48].

To suppress the RB, we apply the following veto criteria [42] as *basic cuts*:

- events must contain exactly one hard electron, one hard jet, and \cancel{E}_T ,
- events containing any extra jets with $p_T^j > 3$ GeV and $|\eta_j| < 2$ or leptons with $p_T^{e,\mu} > 5$ GeV or tagged τ jets are vetoed.

Fig. 2 and Fig. 3 depict the normalized distributions of the missing transverse energy \cancel{E}_T , invariant mass of tagged electron and jet system $M(e^-, j)$, and inelasticity variable y for both signal and backgrounds after the *basic cuts*, at the 140 GeV \otimes 7 TeV LHeC and 60 GeV \otimes 50 TeV FCC-ep, respectively. For the signal, we assume benchmark values of $m_{\chi, \phi} = 1$ GeV, $C_{B, W} = 1$, and $\Lambda = 500$ GeV. For the inelasticity variable y , we follow the definition in Ref. [41], which is given as

$$y \equiv \frac{k_p \cdot (k_e - p_e)}{k_p \cdot k_e}, \quad (16)$$

where $k_{p, e}$ are the 4-momenta of the initial proton and electron, and p_e is the 4-momenta of the final electron.

We can observe the following characteristics:

- for \cancel{E}_T distribution, the SM RB tends to have a smaller value, $\cancel{E}_T < 100$ GeV, compared with signals, whereas the SM IB has values similar to those of signals,
- for y distribution, the SM RB and IB tend to distribute at small and large y values, respectively, whereas signals exhibit a relatively flat distribution.

Such distinct behaviors of signals and SM backgrounds indicate that we can impose the following kinematical cuts for the LHeC (FCC-ep) to further extract signals:

$$\begin{aligned} \cancel{E}_T &> 100 \quad (220) \text{ GeV}, \\ M(e^-, j) &> 100 \quad (200) \text{ GeV}, \\ 0.3 < y < 0.8 \quad (0.1 < y < 0.9). \end{aligned} \quad (17)$$

Table 1 and Table 2 show the cut-flows for the fermion and scalar DM signals and backgrounds at the LHeC and FCC-ep, respectively. The corresponding significance $S = N_S / \sqrt{N_B}$ and signal-to-background ratio $\mathcal{R} = N_S / N_B$ with the total integrated luminosity $L = 2 \text{ ab}^{-1}$ are

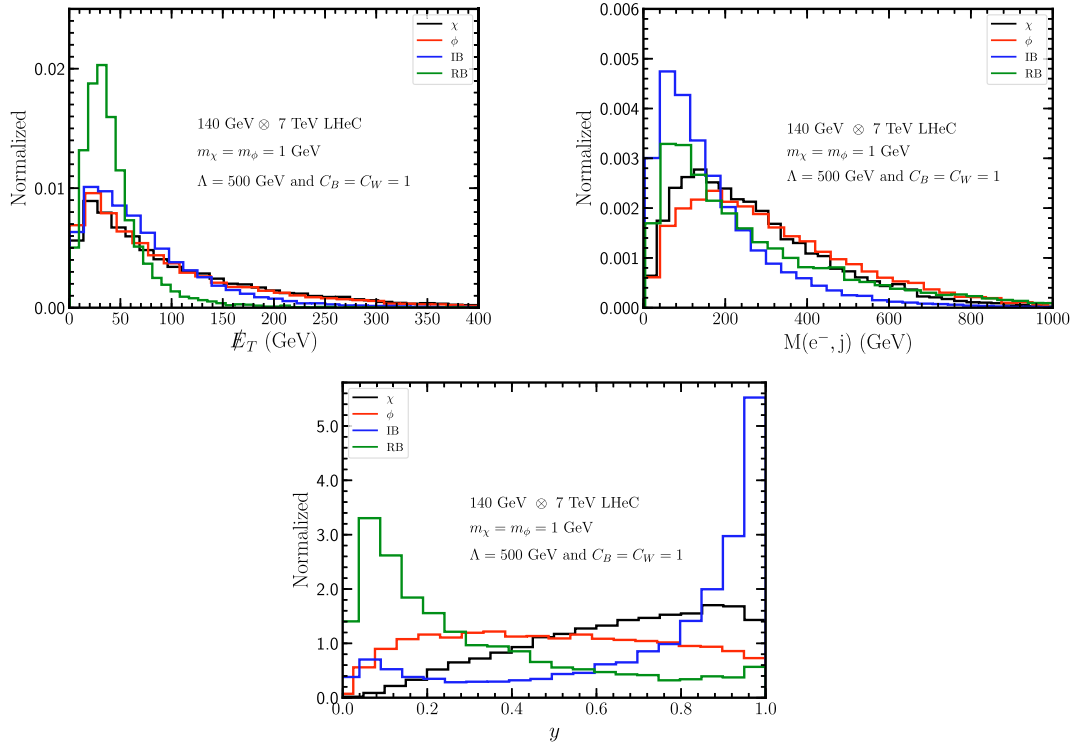


Fig. 2. (color online) Normalized distributions of the missing transverse energy \cancel{E}_T (left), invariant mass of electron-jet system $M(e^-, j)$ (middle), and inelasticity variable y (right) with $m_{\chi} = m_{\phi} = 1$ GeV, $\Lambda = 500$ GeV, and $C_B = C_W = 1$ at the 140 GeV \otimes 7 TeV LHeC. The red and black curves correspond to scalar and fermion DM signals, respectively, and the green and blue lines show the SM RB and IB, respectively.

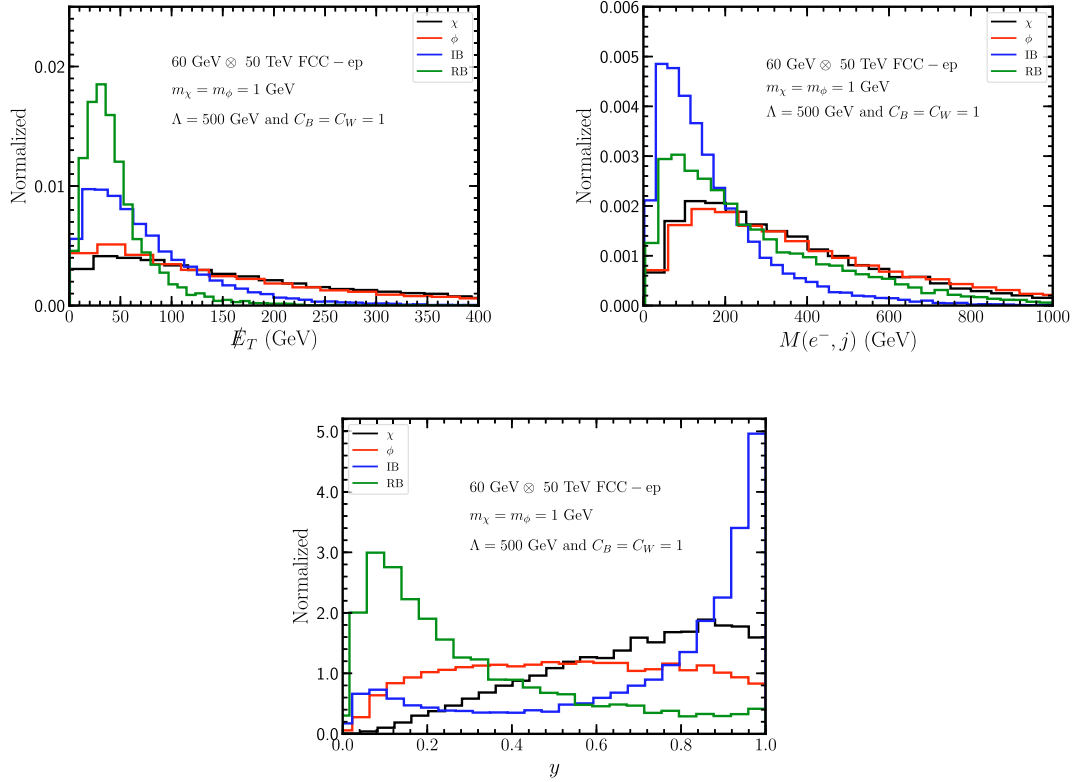


Fig. 3. (color online) Same as Fig. 2 but at the 60 GeV \otimes 50 TeV FCC-ep.

Table 1. Remaining cross-section (in units of fb) of the signal and background after corresponding cuts with $m_{\chi,\phi} = 1$ GeV, $C_{B,W} = 1$, and $\Lambda = 500$ GeV at the 140 GeV \otimes 7 TeV LHeC. The corresponding significance $\mathcal{S} = N_S / \sqrt{N_B}$ and signal-to-background ratio $\mathcal{R} = N_S / N_B$ were obtained for $L = 2 \text{ ab}^{-1}$, where N_S and N_B are the numbers of signal and background events, respectively.

Process	Signal (ϕ)	Signal (χ)	RB	IB	\mathcal{S}_ϕ	\mathcal{S}_χ	\mathcal{R}_ϕ	\mathcal{R}_χ
<i>pre-selection cuts</i>	7.57	10.28	1421.87	260.39	8.26	11.20	0.0045	0.0061
<i>basic cuts</i>	4.91	6.84	316.83	155.21	10.11	14.08	0.010	0.014
$\cancel{E}_T > 100 \text{ GeV}$	1.71	2.62	18.28	38.33	10.16	15.58	0.030	0.046
$M(e^-, j) > 100 \text{ GeV}$	1.56	2.33	15.46	29.28	10.46	15.56	0.035	0.052
$0.3 < y < 0.8$	1.01	1.54	5.40	9.16	11.80	18.05	0.070	0.106

also shown, where $N_{S,B} = \sigma_{S,B} \cdot L$ are the surviving event numbers of signals and backgrounds, respectively. Both \mathcal{S} and \mathcal{R} increase when each cut is imposed. After the *pre-selection cuts*, RB contribution is still large, whereas the *basic cuts* suppress the RB by a factor of 4.5 (5.0) at the LHeC (FCC-ep). Moreover, the RB is dramatically reduced by the \cancel{E}_T cut, which only survives about 1.26% (0.07%) at the LHeC (FCC-ep).

At the LHeC, after all cuts, the fermion (scalar) DM signal can survive 13.2% (14.9%), whereas the RB (IB) only survives 0.37% (3.5%). At the FCC-ep, the signal for fermion (scalar) DM survived 13.3% (14.6%), and the RB (IB) ultimately survives 0.047% (0.65%). Note that the remaining cross-section of the background at the FCC-ep is only 14% of ones that at the LHeC, whereas the signal for fermion (scalar) DM production at the

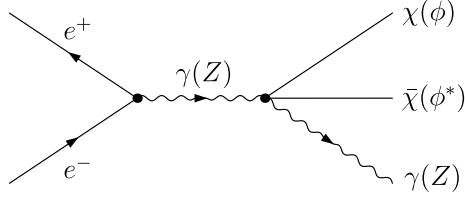
FCC-ep can reach 6 (1.5) times that at the LHeC, which implies that the FCC-ep exhibits a considerable improvement in significance compared with the LHeC.

IV. SENSITIVITY AT THE CEPC IN THREE DIFFERENT MODES

Owing to the effective DM-diboson operators in Eqs. (1) and (2), a WIMP can be produced at e^+e^- colliders via the process $e^+e^- \rightarrow V^{**} \rightarrow \phi\phi^*(\bar{\chi}\chi) + V$ ($V = \gamma, Z$), which results in mono-photon or mono-Z signatures. The corresponding Feynman diagrams are shown in Fig. 4. In this section, we focus on the mono-photon signature at the future projected CEPC [49, 50] with three different running modes: the Higgs factory mode for a seven year run at $\sqrt{s} = 240 \text{ GeV}$ with a total luminosity of $\sim 5.6 \text{ ab}^{-1}$, the

Table 2. Same as Table 1 but at the 60 GeV \otimes 50 TeV FCC-ep.

Process	Signal (ϕ)	Signal (χ)	RB	IB	S_ϕ	S_χ	\mathcal{R}_ϕ	\mathcal{R}_χ
<i>pre-selection cuts</i>	18.17	64.85	1232.28	222.80	21.31	76.03	0.012	0.045
<i>basic cuts</i>	11.56	42.58	244.95	125.09	26.87	98.98	0.031	0.12
$\cancel{E}_T > 220$ GeV	3.10	13.44	0.86	4.32	60.88	264.17	0.060	2.60
$M(e^-, j) > 200$ GeV	2.59	10.71	0.61	2.13	70.21	289.95	0.95	3.92
$0.1 < y < 0.9$	2.41	9.48	0.57	1.44	75.94	298.87	1.19	4.71

**Fig. 4.** Feynman diagrams for the process $e^+e^- \rightarrow \phi\phi^*(\chi\chi) + Z$ or $e^+e^- \rightarrow \phi\phi^*(\chi\chi) + \gamma$.

Z factory mode for a two year run at $\sqrt{s} = 91.2$ GeV with a total luminosity of ~ 16 ab^{-1} , and the W^+W^- threshold scan mode for a one year run at $\sqrt{s} \sim 158 - 172$ GeV with a total luminosity of ~ 2.6 ab^{-1} .¹⁾

For the monophoton signature at the CEPC, an irreducible background results from the neutrino production $e^+e^- \rightarrow \nu_l \bar{\nu}_l \gamma$ processes, where $\nu_l = \nu_e, \nu_\mu, \nu_\tau$. Owing to the Breit-Wigner distribution of the Z boson in the irreducible BG, a resonance occurs in the final photon energy spectrum, which is located at

$$E_\gamma^Z = \frac{s - M_Z^2}{2\sqrt{s}} \quad (18)$$

with a full-width-at-half-maximum of $\Gamma_\gamma^Z = M_Z \Gamma_Z / \sqrt{s}$. To suppress the irreducible background contribution, we veto the events within $5\Gamma_\gamma^Z$ at the Z resonance in the mono-photon energy spectrum [27]. The vetoing cut can be expressed as

$$|E_\gamma - E_\gamma^Z| < 5\Gamma_\gamma^Z. \quad (19)$$

The main reducible SM backgrounds result from the $e^+e^- \rightarrow \gamma + \cancel{X}$ processes, where only one photon is visible in the final state, and \cancel{X} denotes the other undetectable particle(s) owing to the limited detection capability of the detectors. In our analysis, the parameters for the EMC coverage, $|\cos\theta| < 0.99$ and $E > 0.1$ GeV, are adopted based on CEPC CDR [50]. The processes $e^+e^- \rightarrow f\bar{f}\gamma$ and $e^+e^- \rightarrow \gamma\gamma\gamma$ provide dominant contributions to the reducible background when the final $f\bar{f}$ and $\gamma\gamma$ are emitted with $|\cos\theta| > 0.99$. Owing to the momentum conserva-

tion in the transverse direction and energy conservation, the maximum photon energy as a function of its polar angle can be obtained as [27]

$$E_\gamma^m(\theta_\gamma) = \sqrt{s} \left(\frac{\sin\theta_\gamma}{\sin\theta_b} \right)^{-1}, \quad (20)$$

where the polar angle θ_b corresponds to the boundary of the EMC with $|\cos\theta| < 0.99$. To suppress the mono-photon events resulting from the reducible background, we adopt the detector cut $E_\gamma > E_\gamma^m(\theta_\gamma)$ on the final state photon in our analysis.

V. UPDATE LIMITS FROM THE LHC MONO- j AND MONO- γ SEARCHES

Through the DM-diboson operators, a WIMP can be produced via the processes $qq' \rightarrow V^{**} \rightarrow \phi\phi^*(\chi\chi) + V$ ($V = \gamma, Z, W$), which can exhibit a mono-photon ($\cancel{E}_T + \gamma$) or mono-jet ($\cancel{E}_T + W/Z \rightarrow \text{hadrons}$) signature, respectively. The representative Feynman diagrams are shown in Fig. 5. Moreover, the loop-induced effective DM-quarks (\mathcal{O}_q) and DM-gluons (\mathcal{O}_G) operators can result in the mono-jet signature via the $q\bar{q} \rightarrow \chi\chi + g$, $gg \rightarrow \chi\chi + g$, and $qg \rightarrow \chi\chi + q$ processes. The representative Feynman diagrams are shown in Fig. 6.

In this section, we consider the sensitivities from LHC mono- j and mono- γ searches. To simulate the signal from dark matter, we generate the parton-level events using MadGraph@NLO [45], and the subsequent parton shower and hadronization are generated using Pythia6.4 [46]. We use Delphes3.4 [47] to conduct a rapid detector simulation for the ATLAS or CMS detector with the corresponding parameter setup. We follow the procedure of the latest mono-photon [51] and mono-jet [52] analysis by the ATLAS Collaboration with an integrated luminosity of 139 fb^{-1} at a center-of-mass energy of 13 TeV.

For the $\cancel{E}_T + \gamma$ search channel, events in our analysis are required to have a leading γ with $E_T^\gamma > 150$ GeV, $|\eta^\gamma| < 1.37$ or $1.52 < |\eta^\gamma| < 2.37$, $\Delta\phi(\gamma, \mathbf{E}_T^{\text{miss}}) > 0.4$, 0 or 1 jet with $p_T > 30$ GeV, $|\eta| < 4.5$ and $\Delta\phi(\text{jet}, \mathbf{E}_T^{\text{miss}}) > 0.4$, and no leptons. Moreover, the ATLAS Collaboration per-

1) We take $\sqrt{s} = 160$ GeV for the W^+W^- threshold scan mode throughout our analysis.



Fig. 5. Representative Feynman diagrams for mono-photon (left) and mono-jet (right) signatures resulting from DM-diboson operators.

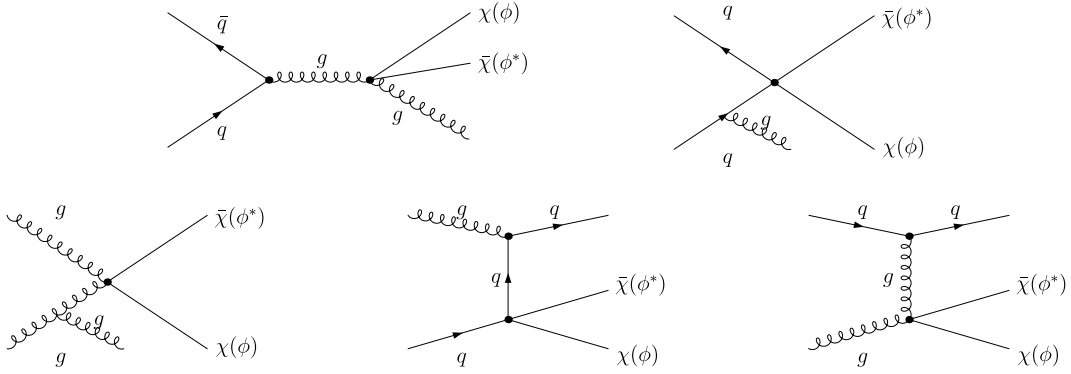


Fig. 6. Representative Feynman diagrams for a mono-jet signature resulting from loop-induced effective DM-quarks and DM-gluons operators.

forms the measurement in seven different signal regions with a varying cut on the missing transverse momentum E_T^{miss} . We observe that the strongest bounds on the parameter space in our case are given with the most severe cut of $E_T^{\text{miss}} > 375$ GeV. The corresponding 95% C.L. limit on the fiducial cross-section is $\sigma_{\text{fid}} < 0.53$ fb.

For mono-jet search, events with identified muons, electrons, photons, or τ -leptons in the final state are vetoed. Selected events have a leading jet with $p_T > 150$ GeV and $|\eta| < 2.4$, and up to three additional jets with $p_T > 30$ GeV and $|\eta| < 2.8$. Separation in the azimuthal angle between the missing transverse momentum direction and each selected jet $\Delta\phi(\text{jet}, E_T^{\text{miss}}) > 0.4(0.6)$ is required for events with $E_T^{\text{miss}} > 250$ GeV ($200 \text{ GeV} < E_T^{\text{miss}} < 250$ GeV). We observe that the stronger restriction of $E_T^{\text{miss}} > 1200$ GeV provides the best limits. At 95% C.L., the bound on the corresponding fiducial cross section is given by $\sigma_{\text{fid}} < 0.3$ fb.

Table 3 presents the ratio of the number of events for mono-jet signature at LHC from the process $pp \rightarrow \chi\bar{\chi} + W/Z (\rightarrow \text{hardons})$ via dimension-7 DM-diboson operators with the Feynman diagrams shown in Fig. 5 to one from the process $pp \rightarrow \chi\bar{\chi} + q/g$ via loop-induced DM-quarks and DM-gluons operators with the Feynman diagrams shown in Fig. 6 with $\Lambda=1000$ GeV. Here, we consider three cases, i.e., $C_B = C_W = 500$, $C_B = 0, C_W = 500$, and $C_B = 500, C_W = 0$. We observe that all the ratios in the three cases increase with an increment in the DM mass. Furthermore, the contributions from tree-level DM-diboson operators to the mono-jet signature at the LHC are about two orders of magnitude above those from

Table 3. Ratio of the number of events for the mono-jet signature at the LHC from the process $pp \rightarrow \chi\bar{\chi} + W/Z (\rightarrow \text{hardons})$ via DM-diboson operators with the Feynman diagrams shown in Fig. 5 to $pp \rightarrow \chi\bar{\chi} + q/g$ via loop-induced DM-quarks and DM-gluons operators with the Feynman diagrams shown in Fig. 6 at $\Lambda=1000$ GeV.

m_χ	1	300	800	2000	3000
$C_B = 500, C_W = 0$	638.22	699.35	752.11	1435.32	2733.95
$C_B = 0, C_W = 500$	95.00	99.55	104.29	181.55	302.49
$C_B = 500, C_W = 500$	79.20	80.33	91.64	158.94	271.41

loop-induced DM-quarks and DM-gluons operators, especially for $C_B = 1, C_W = 0$, with the contributions being about three orders higher; thus, we ignore the contributions from DM-quarks and DM-gluons operators in the following analysis.

VI. RELIC ABUNDANCE: DIRECT AND INDIRECT CONSTRAINTS

In this section, we discuss the bounds on Λ from current direct and indirect search experiments. The effective operators \mathcal{O}_B and \mathcal{O}_W lead to the non-relativistic cross-sections of DM annihilation $\chi\bar{\chi}, \phi\phi^* \rightarrow \gamma\gamma/\gamma Z/ZZ/WW$ as follows:

$$\langle\sigma_k v\rangle = a_k + b_k v^2 + O(v^4) \quad (21)$$

with $k = B, W$ annihilation channels. The coefficients of a and b are [37]

$$\chi \left\{ \begin{array}{l} a_B = a_W = 0, \\ b_B = \frac{|C_B(\Lambda)|^2 m_\chi^4}{\pi \Lambda^6} \left[c_w^4 + \frac{c_w^2 s_w^2}{8} \beta_{\gamma Z}^2 (x_Z - 4)^2 \Theta(M_Z < 2m_\chi) + \frac{s_w^4}{8} \beta_{ZZ} (3x_Z^2 - 8x_Z + 8) \Theta(M_Z < m_\chi) \right], \\ b_W = \frac{|C_W(\Lambda)|^2 m_\chi^4}{\pi \Lambda^6} \left[s_w^4 + \frac{c_w^2 s_w^2}{8} \beta_{\gamma Z}^2 (x_Z - 4)^2 \Theta(M_Z < 2m_\chi) + \frac{c_w^4}{8} \beta_{ZZ} (3x_Z^2 - 8x_Z + 8) \Theta(M_Z < m_\chi) \right. \\ \left. + \frac{1}{4} \beta_{WW} (3x_W^2 - 8x_W + 8) \Theta(M_W < m_\chi) \right], \end{array} \right. \quad (22)$$

$$\phi \left\{ \begin{array}{l} a_B = \frac{|C_B(\Lambda)|^2 2m_\phi^2}{\pi \Lambda^4} \left[c_w^4 + \frac{c_w^2 s_w^2}{8} \beta_{\gamma Z}^2 (x_Z - 4)^2 \Theta(M_Z < 2m_\phi) + \frac{s_w^4}{8} \beta_{ZZ} (3x_Z^2 - 8x_Z + 8) \Theta(M_Z < m_\phi) \right], \\ a_W = \frac{|C_W(\Lambda)|^2 2m_\phi^2}{\pi \Lambda^4} \left[s_w^4 + \frac{c_w^2 s_w^2}{8} \beta_{\gamma Z}^2 (x_Z - 4)^2 \Theta(M_Z < 2m_\phi) + \frac{c_w^4}{8} \beta_{ZZ} (3x_Z^2 - 8x_Z + 8) \Theta(M_Z < m_\phi) \right. \\ \left. + \frac{1}{4} \beta_{WW} (3x_W^2 - 8x_W + 8) \Theta(M_W < m_\phi) \right], \\ b_B = \frac{|C_B(\Lambda)|^2 2m_\phi^2}{\pi \Lambda^4} \left[c_w^4/2 + \frac{c_w^2 s_w^2}{4} \beta_{\gamma Z}^2 (x_Z - 4) \Theta(M_Z < 2m_\phi) + s_w^4 \beta_{ZZ} (1/2 - x_Z) \Theta(M_Z < m_\phi) \right], \\ b_W = \frac{|C_W(\Lambda)|^2 2m_\phi^2}{\pi \Lambda^4} \left[s_w^4/2 + \frac{c_w^2 s_w^2}{4} \beta_{\gamma Z}^2 (x_Z - 4) \Theta(M_Z < 2m_\phi) + c_w^4 \beta_{ZZ} (1/2 - x_Z) \Theta(M_Z < m_\phi) \right. \\ \left. + \beta_{WW} (1 - 2x_Z) \Theta(M_W < m_\phi) \right]. \end{array} \right. \quad (23)$$

In above equations, we have defined the phase space factor $\beta_{ij} = \sqrt{1 - (m_i + m_j)^2 / (4m_{\text{DM}}^2)}$ and $x_i = m_i^2 / m_{\text{DM}}^2$ with $\text{DM} = \chi, \phi$. Using the results for $a_{B,W}$ and $b_{B,W}$, the relic density can then be calculated using

$$\Omega_{\text{DM}} h^2 = \frac{1.09 \times 10^9 x_F \text{GeV}^{-1}}{M_{\text{Pl}} \sqrt{g_*(x_F)} (a + 3b/x_F)}, \quad (24)$$

where $a = a_B + a_W$ and $b = b_B + b_W$. $x_F = m_{\text{DM}}/T_F$ is the ratio of the mass of DM m_{DM} and the early-universe freeze-out temperature T_F , which can be obtained by solving

$$x_F = \ln \left[c(c+2) \sqrt{\frac{45 m_{\text{DM}} M_{\text{Pl}} (a + 6b/x_F)}{8 \cdot 2\pi^3 \sqrt{g_*(x_F)}}} \right]. \quad (25)$$

The loop-induced effective DM-quarks (\mathcal{O}_q) and DM-gluons (\mathcal{O}_G) operators can result in the interaction between DM and nucleons. The spin-independent (SI) cross section for elastic scalar and Dirac WIMP scattering on a nucleon has the form

$$\sigma_{\text{SI}}^\phi \simeq \frac{\mu_N^2 m_N^2}{\pi m_\phi^2 \Lambda^4} \left| \frac{\alpha Z^2}{A} f_A^N C_{AA}(\mu_{\text{had}}) + \frac{Z}{A} f_p(\mu_{\text{had}}) + \frac{A-Z}{A} f_n(\mu_{\text{had}}) \right|^2, \quad (26)$$

$$\sigma_{\text{SI}}^\chi \simeq \frac{\mu_N^2 m_N^2}{\pi \Lambda^6} \left| \frac{\alpha Z^2}{A} f_A^N C_{AA}(\mu_{\text{had}}) + \frac{Z}{A} f_p(\mu_{\text{had}}) + \frac{A-Z}{A} f_n(\mu_{\text{had}}) \right|^2. \quad (27)$$

In above equations, $m_N \simeq 0.939$ GeV is the average nucleon mass, and $\mu_N = m_{\phi,\chi} m_N / (m_{\phi,\chi} + m_N)$ is the reduced mass of the DM-nucleon system. The form factor f_A^N describes the Rayleigh scattering of two photons on the entire nucleus. At a zero-momentum transfer limit, $f_A^N \simeq 0.08$ for a xenon target. The form factor $f_{N=p,n}$ describing the couplings between the DM and nucleon is expressed as [40, 53]

$$f_N(\mu_{\text{had}}) = \sum_{q=u,d,s} f_q^N C_q(\mu_{\text{had}}) - \frac{8\pi}{9} f_G^N C_G(\mu_{\text{had}}), \quad (28)$$

where the form factors f_q^N describing the scalar couplings between quarks and nucleon are given by [54]

$$\begin{aligned} f_d^p &= 0.0191, & f_u^p &= 0.0153, & f_d^n &= 0.0273, \\ f_u^n &= 0.0110, & f_s^p &= f_s^n &= 0.0447, \end{aligned} \quad (29)$$

and

$$f_G^N = 1 - \sum_{q=u,d,s} f_q^N. \quad (30)$$

VII. RESULTS

We apply simple χ^2 analysis to derive the lower bounds on Λ for effective operators in Eq. (5) at the future LHeC, FCC-ep, and CEPC at 95% C.L. by requiring $\chi^2 = N_S^2/N_B = 3.84$ [55] with the specified luminosities. For LHeC and FCC-ep, the total integrated luminosities are assumed as $L = 2 \text{ ab}^{-1}$. The limits of Λ as a function of the mass of Dirac fermion and scalar DM are shown in Figs. 7 and 8, respectively. We also present the exclusion limits derived from the mono-photon [51] search and mono-jet [52] search at the LHC and from the direct DM experiments XENON1T [56, 57], XENONnT [58], and PandaX-4T [59]. For illustration, we plot the contours of the relic abundance $\Omega_{\text{DM}} h^2 = 0.1186 \pm 0.0020$. The neutrino floor is also shown, which represents the WIMP-discovery limit obtained using an assumed exposure of 1000 ^8B neutrinos detected on a xenon target [60]. For the scal-

ar DM, we also show the constraints from the DM indirect searches through the gamma-ray and WW observations by the Fermi-LAT Collaboration [61]. Here, we consider three typical cases, i.e., $C_B = 0, C_W = 500$, $C_B = 500, C_W = 0$, and $C_B = C_W = 500$.

For fermion DM, the bounds from the CEPC with all the three running modes can touch the neutrino floor with the DM mass less than a few GeV, whereas the e^+e^- collider CEPC is not competitive with other ep and pp colliders. At the LHC, the sensitivity from mono-jet search is better with $C_B = 0, C_W = 500$, and $C_B = C_W = 500$ but is slightly worse with $C_B = 500, C_W = 0$ than the mono-photon search. Moreover, the LHC mono-jet search can provide the best constraint with $C_B = 0, C_W = 500$ compared with other collider experiments. The figures further validate that the FCC-ep has significant advantages to constrain DM-gauge boson effective interactions compared with the LHeC, as mentioned earlier. For $C_B = 500, C_W = 0$, and $C_B = C_W = 500$, the FCC-ep can incorporate the region unconstrained by other experiments when the DM mass is less than several hundred GeV and

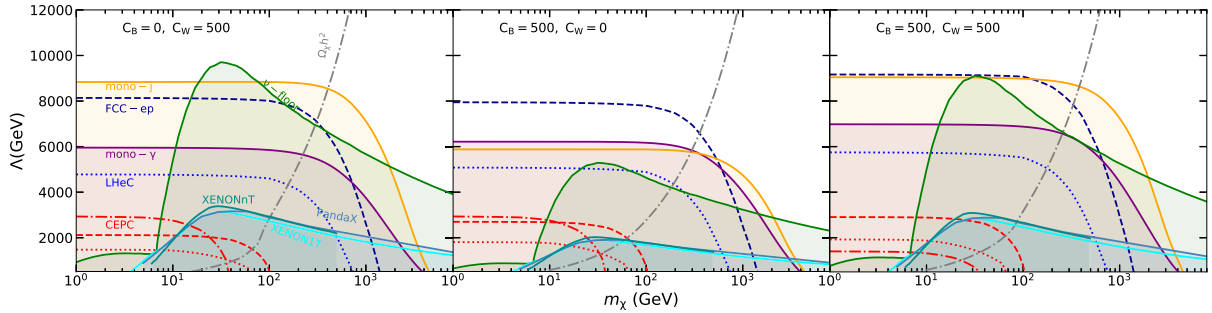


Fig. 7. (color online) Constraints in the $m_\chi - \Lambda$ plane for the fermion DM with $C_B^{6(7)} = 0, C_W^{6(7)} = 500$ (left panel), $C_B^{6(7)} = 500, C_W^{6(7)} = 0$ (middle panel), and $C_B^{6(7)} = 500, C_W^{6(7)} = 500$ (right panel). The purple and orange solid lines denote the exclusion limits from the mono-photon [51] and mono-jet [52] searches at the 95% C.L. at the 13 TeV LHC, respectively. For the direct searches, recent bounds from XENON1T [56, 57], XENONnT [58], and PandaX-4T [59] are shown as cyan, dark cyan, and steel blue solid lines, respectively. For illustration, the contours of the relic abundance $\Omega_{\text{DM}} h^2 = 0.1186$ are also plotted as gray dash-dotted curves. The neutrino floor is shown as green-shaded regions. The expected 95% C.L. bounds at the future LHeC (blue dotted lines), FCC-ep (dark blue dashed lines), and CEPC (red dotted lines for Z factory mode, red dash-dotted lines for W^+W^- threshold scan mode, red dashed lines for Higgs factory mode) are shown.

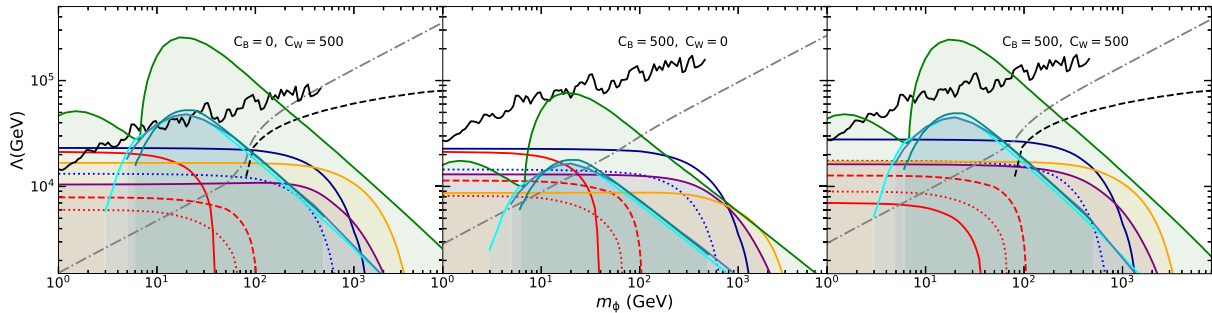


Fig. 8. (color online) Same as Fig. 7 but in the $m_\phi - \Lambda$ plane for the fermion DM. The constraints from the indirect search of DM through the cosmic gamma-ray (black solid line) and WW (black dashed line) observations by the Fermi-LAT collaboration [61] are also shown.

extend the limits up to about 8000 and 9000 GeV, respectively.

For scalar DM, in the case of $C_B = 0, C_W = 500$, all the collider searches cannot escape the neutrino floor, whereas the indirect searches of DM by the Fermi-LAT Collaboration provide the leading constraints and can include the neutrino floor in the mass regions of $5 \text{ GeV} \lesssim m_\phi \lesssim 7 \text{ GeV}$ and $m_\phi \gtrsim 130 \text{ GeV}$ with gamma-ray observation and $m_\phi \gtrsim 280 \text{ GeV}$ with WW observation. For $C_B = 500, C_W = 500$, the FCC-ep can reach the neutrino floor in the mass region of $5 \text{ GeV} \lesssim m_\phi \lesssim 6 \text{ GeV}$, whereas other collider searches cannot escape the neutrino floor. Similar to the case of $C_B = 0, C_W = 500$, DM searches by the Fermi-LAT Collaboration can reach the neutrino floor for $3 \text{ GeV} \lesssim m_\phi \lesssim 7 \text{ GeV}$ and $m_\phi \gtrsim 80 \text{ GeV}$ with cosmic gamma-ray observation and $m_\phi > 250 \text{ GeV}$ with WW observation. For $C_B = 500, C_W = 0$, the cosmic gamma-ray observation by the Fermi-LAT Collaboration almost lies above the neutrino floor in the plotted region, and WW observation cannot provide any constraint because $\phi\phi W^+ W^-$ coupling vanishes. For the collider searches, the future FCC-ep provides the most stringent restrictions relative to the other colliders for all the considered three cases with m_ϕ less than a few hundred GeV. Moreover, for $C_B = 500, C_W = 0$, the FCC-ep and CEPC in the Z factory mode can probe a light DM ($m_\phi \lesssim 7 \text{ GeV}$) reaching the neutrino floor.

VIII. SUMMARY AND CONCLUSION

In this study, we focus on the constraints on dimension-6 (7) effective operators between scalar (Dirac fermion) DM and SM gauge bosons at future ep colliders LHeC and FCC-ep via the $\cancel{E}_T + e^- j$ signature for the first time. We observe that SM irreducible and reducible backgrounds can be effectively suppressed by imposing appropriate kinematic cuts. We also consider the sensitivity at the future e^+e^- collider CEPC under three different modes with a mono-photon signature and update the limits from the LHC with current mono- j and mono- γ searches. In addition to the contribution from $\cancel{E}_T + W/Z$ (\rightarrow hadrons) channel due to the DM-diboson operators for mono- j at LHC, we investigate the contribution from the loop induced effective DM-quarks and DM-gluons operators. We observe that the contribution from DM-quarks and DM-gluons operators can be ignored. We present the constraints on the effective energy scale Λ as a function of DM mass with three typical cases of Wilson coefficients: $C_B^{6(7)} = C_W^{6(7)} = 500$, $C_B^{6(7)} = 0, C_W^{6(7)} = 500$, and $C_B^{6(7)} = 500, C_W^{6(7)} = 0$. The FCC-ep exhibits better sensitivity than the LHeC in all cases for scalar and Dirac fermion DM. We observe that the collider searches can probe light DM reaching the neutrino floor.

References

- [1] N. Aghanim *et al.* (Planck), *Astron. Astrophys.* **641**, A6 (2020) [Erratum: *Astron. Astrophys.* **652**, C4 (2021)], arXiv:1807.06209[astro-ph.CO]
- [2] B. W. Lee and S. Weinberg, *Phys. Rev. Lett.* **39**, 165 (1977)
- [3] G. Jungman, M. Kamionkowski, and K. Griest, *Phys. Rept.* **267**, 195 (1996), arXiv:hep-ph/9506380[hep-ph]
- [4] G. Bertone, D. Hooper, and J. Silk, *Phys. Rept.* **405**, 279 (2005), arXiv:hep-ph/0404175[hep-ph]
- [5] J. Goodman, M. Ibe, A. Rajaraman *et al.*, *Phys. Rev. D* **82**, 116010 (2010), arXiv:1008.1783[hep-ph]
- [6] P. J. Fox, R. Harnik, J. Kopp *et al.*, *Phys. Rev. D* **85**, 056011 (2012), arXiv:1109.4398[hep-ph]
- [7] A. Rajaraman, W. Shepherd, T. M. P. Tait *et al.*, *Phys. Rev. D* **84**, 095013 (2011), arXiv:1108.1196[hep-ph]
- [8] R. Ding, Y. Liao, J. Y. Liu *et al.*, *JCAP* **05**, 028 (2013), arXiv:1302.4034[hep-ph]
- [9] Q. H. Cao, C. R. Chen, C. S. Li *et al.*, *JHEP* **08**, 018 (2011), arXiv:0912.4511[hep-ph]
- [10] A. Nelson, L. M. Carpenter, R. Cotta *et al.*, *Phys. Rev. D* **89**(5), 056011 (2014), arXiv:1307.5064[hep-ph]
- [11] A. Crivellin, U. Haisch, and A. Hibbs, *Phys. Rev. D* **91**, 074028 (2015), arXiv:1501.00907[hep-ph]
- [12] N. F. Bell, J. B. Dent, A. J. Galea *et al.*, *Phys. Rev. D* **86**, 096011 (2012), arXiv:1209.0231[hep-ph]
- [13] L. M. Carpenter, A. Nelson, C. Shimmin *et al.*, *Phys. Rev. D* **87**(7), 074005 (2013), arXiv:1212.3352[hep-ex]
- [14] A. Alves and K. Sinha, *Phys. Rev. D* **92**(11), 115013 (2015), arXiv:1507.08294[hep-ph]
- [15] M. Song, G. Li, W. G. Ma *et al.*, *JHEP* **09**, 069 (2014), arXiv:1403.2142[hep-ph]
- [16] N. Lopez, L. M. Carpenter, R. Cotta *et al.*, *Phys. Rev. D* **89**(11), 115013 (2014), arXiv:1403.6734[hep-ph]
- [17] L. Carpenter, A. DiFranzo, M. Mulhearn *et al.*, *Phys. Rev. D* **89**(7), 075017 (2014), arXiv:1312.2592[hep-ph]
- [18] A. Berlin, T. Lin, and L. T. Wang, *JHEP* **06**, 078 (2014), arXiv:1402.7074[hep-ph]
- [19] C. Bartels, M. Berggren, and J. List, *Eur. Phys. J. C* **72**, 2213 (2012), arXiv:1206.6639[hep-ex]
- [20] Y. J. Chae and M. Perelstein, *JHEP* **05**, 138 (2013), arXiv:1211.4008[hep-ph]
- [21] H. Dreiner, M. Huck, M. Krämer *et al.*, *Phys. Rev. D* **87**(7), 075015 (2013), arXiv:1211.2254[hep-ph]
- [22] Z. H. Yu, Q. S. Yan, and P. F. Yin, *Phys. Rev. D* **88**(7), 075015 (2013), arXiv:1307.5740[hep-ph]
- [23] F. Richard, G. Arcadi, and Y. Mambrini, *Eur. Phys. J. C* **75**, 171 (2015), arXiv:1411.0088[hep-ex]
- [24] F. Rossi-Torres and C. A. Moura, *Phys. Rev. D* **92**(11), 115022 (2015), arXiv:1503.06475[hep-ph]
- [25] M. Habermehl, K. Fujii, J. List *et al.*, *PoS ICHEP2016*, 155 (2016), arXiv:1702.05377[hep-ex]
- [26] M. Jin and Y. Gao, *Eur. Phys. J. C* **78**(8), 622 (2018), arXiv:1712.02140[hep-ph]
- [27] Z. Liu, Y. H. Xu, and Y. Zhang, *JHEP* **06**, 009 (2019), arXiv:1903.12114[hep-ph]
- [28] D. K. Ghosh, T. Katayose, S. Matsumoto *et al.*, *Phys. Rev. D* **101**(1), 015007 (2020), arXiv:1906.06864[hep-ph]

- [29] M. Habermehl, M. Berggren, and J. List, *Phys. Rev. D* **101**(7), 075053 (2020), arXiv:2001.03011[hep-ex]
- [30] N. Wan, M. Song, G. Li *et al.*, *Eur. Phys. J. C* **74**(12), 3219 (2014), arXiv:1403.7921[hep-ph]
- [31] Z. H. Yu, X. J. Bi, Q. S. Yan *et al.*, *Phys. Rev. D* **90**(5), 055010 (2014), arXiv:1404.6990[hep-ph]
- [32] J. Liu, L. T. Wang, X. P. Wang *et al.*, *Phys. Rev. D* **97**(9), 095044 (2018), arXiv:1712.07237[hep-ph]
- [33] K. Kadota and A. Spray, *JHEP* **02**, 017 (2019), arXiv:1811.00560[hep-ph]
- [34] D. d'Enterria, *PoS ICHEP2016*, 434 (2017), arXiv:1701.02663[hep-ex]
- [35] R. C. Cotta, J. L. Hewett, M. P. Le *et al.*, *Phys. Rev. D* **88**, 116009 (2013), arXiv:1210.0525[hep-ph]
- [36] A. Rajaraman, T. M. P. Tait, and A. M. Wijangco, *Phys. Dark Univ.* **2**, 17 (2013), arXiv:1211.7061[hep-ph]
- [37] J. Y. Chen, E. W. Kolb, and L. T. Wang, *Phys. Dark Univ.* **2**, 200 (2013), arXiv:1305.0021[hep-ph]
- [38] A. Crivellin and U. Haisch, *Phys. Rev. D* **90**, 115011 (2014), arXiv:1408.5046[hep-ph]
- [39] M. A. Shifman, A. I. Vainshtein, and V. I. Zakharov, *Phys. Lett. B* **78**, 443 (1978)
- [40] M. T. Frandsen, U. Haisch, F. Kahlhoefer *et al.*, *JCAP* **10**, 033 (2012), arXiv:1207.3971[hep-ph]
- [41] Y. L. Tang, C. Zhang, and S. h. Zhu, *Phys. Rev. D* **94**(1), 011702 (2016), arXiv:1508.01095[hep-ph]
- [42] C. Han, R. Li, R. Q. Pan *et al.*, *Phys. Rev. D* **98**(11), 115003 (2018), arXiv:1802.03679[hep-ph]
- [43] C. Degrande, C. Duhr, B. Fuks *et al.*, *Comput. Phys. Commun.* **183**, 1201 (2012), arXiv:1108.2040[hep-ph]
- [44] A. Alloul, N. D. Christensen, C. Degrande *et al.*, *Comput. Phys. Commun.* **185**, 2250 (2014), arXiv:1310.1921[hep-ph]
- [45] J. Alwall, R. Frederix, S. Frixione *et al.*, *JHEP* **07**, 079 (2014), arXiv:1405.0301[hep-ph]
- [46] T. Sjostrand, S. Mrenna, and P. Z. Skands, *JHEP* **05**, 026 (2006), arXiv:hep-ph/0603175[hep-ph]
- [47] S. Oryn, X. Rouby, and V. Lemaitre, arXiv:0903.2225[hep-ph]
- [48] J. L. Abelleira Fernandez *et al.* (LHeC Study Group), *J. Phys. G* **39**, 075001 (2012), arXiv:1206.2913[physics.acc-ph]
- [49] (CEPC Study Group), arXiv:1809.00285[physics.acc-ph]
- [50] J. B. Guimarães da Costa *et al.* (CEPC Study Group), arXiv:1811.10545[hep-ex]
- [51] G. Aad *et al.* (ATLAS), *JHEP* **02**, 226 (2021), arXiv:2011.05259[hep-ex]
- [52] G. Aad *et al.* (ATLAS), *Phys. Rev. D* **103**(11), 112006 (2021), arXiv:2102.10874[hep-ex]
- [53] N. Weiner and I. Yavin, *Phys. Rev. D* **86**, 075021 (2012), arXiv:1206.2910[hep-ph]
- [54] G. Belanger, F. Boudjema, A. Pukhov *et al.*, *Comput. Phys. Commun.* **185**, 960 (2014), arXiv:1305.0237[hep-ph]
- [55] P. A. Zyla *et al.* (Particle Data Group), *PTEP* **2020**(8), 083C01 (2020)
- [56] E. Aprile *et al.* (XENON), *Phys. Rev. Lett.* **119**(18), 181301 (2017), arXiv:1705.06655[astro-ph.CO]
- [57] E. Aprile *et al.* (XENON), *Phys. Rev. Lett.* **121**(11), 111302 (2018), arXiv:1805.12562[astro-ph.CO]
- [58] E. Aprile *et al.* (XENON), *Phys. Rev. Lett.* **131**(4), 041003 (2023), arXiv:2303.14729[hep-ex]
- [59] Y. Meng *et al.* (PandaX-4T), *Phys. Rev. Lett.* **127**(26), 261802 (2021), arXiv:2107.13438[hep-ex]
- [60] F. Ruppin, J. Billard, E. Figueroa-Feliciano *et al.*, *Phys. Rev. D* **90**(8), 083510 (2014), arXiv:1408.3581[hep-ph]
- [61] M. Ackermann *et al.* (Fermi-LAT), *Phys. Rev. Lett.* **115**(23), 231301 (2015), arXiv:1503.02641[astro-ph.HE]